ADVANCED MATERIALS

Supporting Information

for *Adv. Mater.*, DOI: 10.1002/adma.201607039

Crystallization Kinetics and Morphology Control of Formamidinium–Cesium Mixed-Cation Lead Mixed-Halide Perovskite via Tunability of the Colloidal Precursor Solution

*David P. McMeekin, Zhiping Wang, Waqaas Rehman, Federico Pulvirenti, Jay B. Patel, Nakita K. Noel, Michael B. Johnston, Seth R. Marder, Laura M. Herz, and Henry J. Snaith**

Supplementary Information

Title: Crystallization kinetics and morphology control of formamidinium-cesium mixed-cation lead mixed-halide perovskite via tunability of the colloidal precursor solution

*David P. McMeekin,[1] Zhiping Wang,[1] Waqaas Rehman,[1] Federico Pulvirenti,[2] Jay B. Patel,[1] Nakita K. Noel,[1] Michael B. Johnston,[1] Seth R. Marder,[2] Laura M. Herz,[1] Henry J. Snaith[1]**

[1] Clarendon Laboratory, University of Oxford, Parks Road, Oxford OX1 3PU, UK
[2] School of Chemistry and Biochemistry, Georgia Institute of Technology, 901 Atlantic Drive, Atlanta, GA 30332-0400

* Corresponding author E-mail: henry.snaith@physics.ox.ac.uk

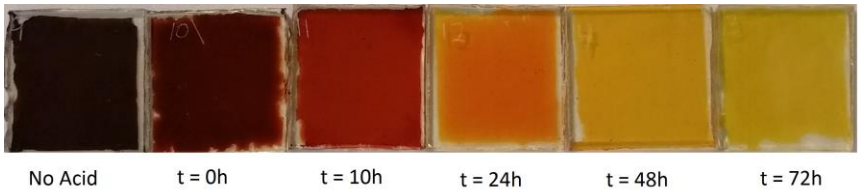

Fig. S1: Impact of colloids in the precursor solution on the nucleation stage of the $FA_{0.83}Cs_{0.17}Pb(Br_{0.2}I_{0.8})_3$ perovskite system. A series of photographs of thin films spin coated and annealed at 70°C under nitrogen, prepared with solutions aged in a N_2 atmosphere for various periods of time after the addition of hydrohalic acids without any hypophosphorous acid (HPA), a reducing agent used as a stabilizer.

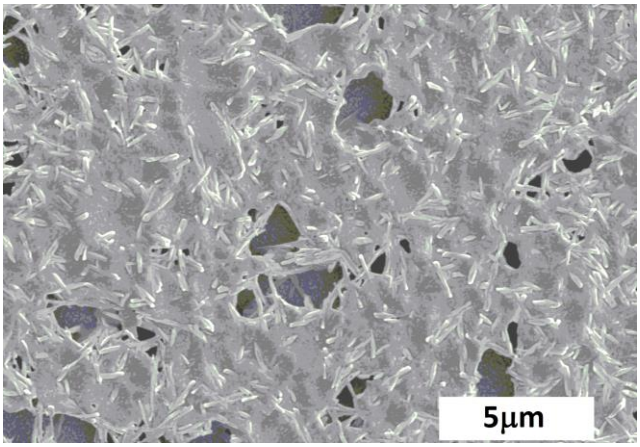

Fig. S2: Scanning electron microscopy (*SEM) image of the top view of an un-annealed $FA_{0.83}Cs_{0.17}Pb(Br_{0.2}I_{0.8})_3$ as cast thin film, prepared with an acid-free perovskite precursor solution.*

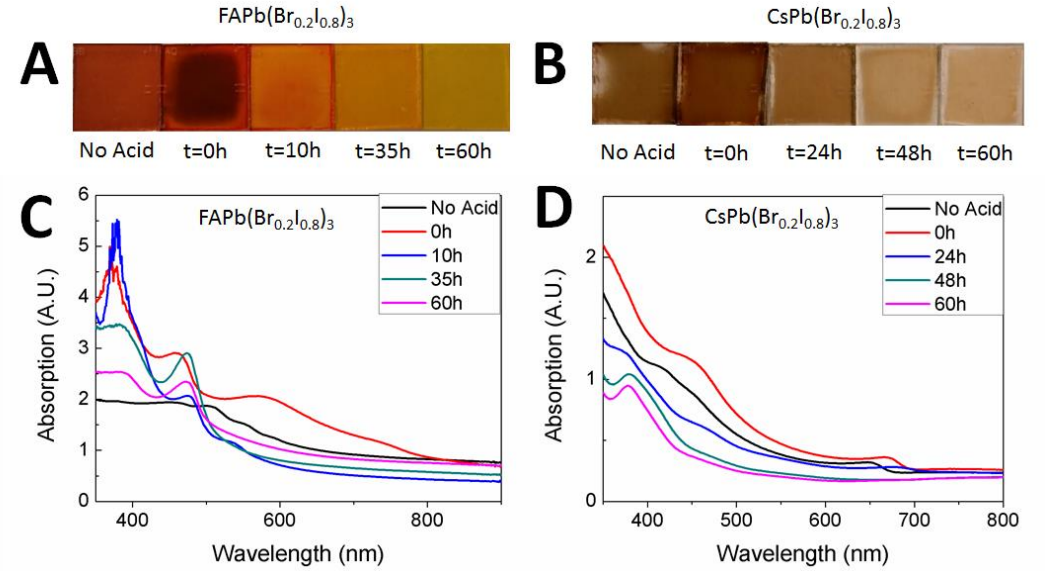

Fig. S3: Impact of colloids in the precursor solution on the nucleation stage of the $FAPb(Br_{0.2}I_{0.8})_3$ and the $CsPb(Br_{0.2}I_{0.8})_3$ perovskite system. A) A series of photographs of $FAPb(Br_{0.2}I_{0.8})_3$ thin films spin coated and annealed at 70°C under nitrogen for 1 minute, prepared with a 1.15M $FAPb(Br_{0.2}I_{0.8})_3$ solutions aged in a N_2 atmosphere for various periods of time after the addition of hydrohalic acid. B) A series of photographs of $CsPb(Br_{0.2}I_{0.8})_3$ thin films spin coated and annealed at 70°C under nitrogen for 5 minutes, prepared with 0.3M $CsPb(Br_{0.2}I_{0.8})_3$ solutions aged in a N_2 atmosphere for various periods of time after the addition of hydrohalic acid. C) Ultraviolet-visible absorbance spectra of corresponding $FAPb(Br_{0.2}I_{0.8})_3$ thin film after the nucleation stage. D) Ultraviolet-visible absorbance spectra of corresponding $CsPb(Br_{0.2}I_{0.8})_3$ thin film after the nucleation stage.

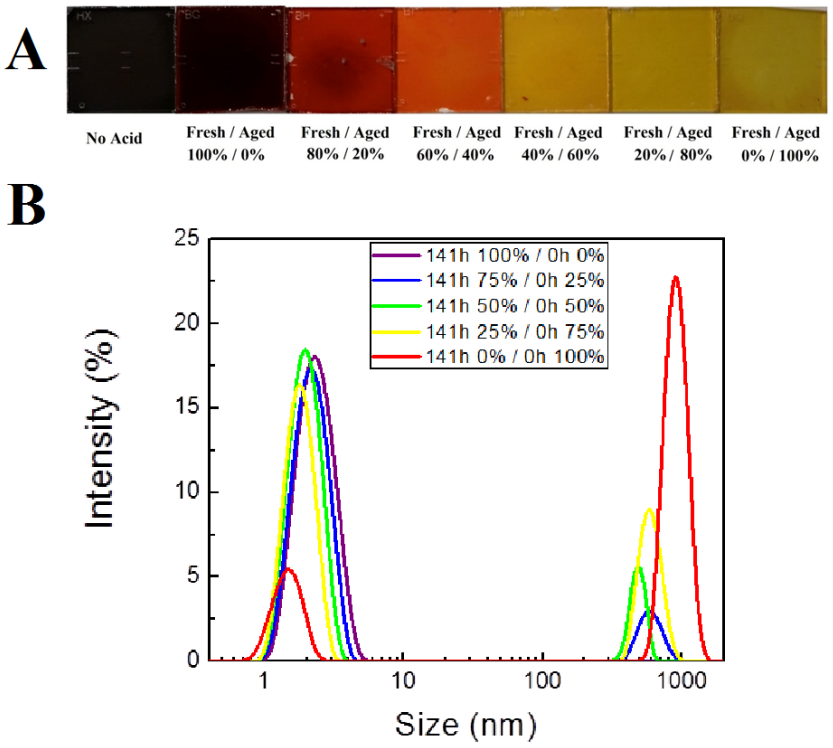

Fig. S4 *Impact of mixing colloidal solutions with colloid-free solution on the nucleation stage of the* $FA_{0.83}Cs_{0.17}Pb(Br_{0.2}I_{0.8})_3$ *perovskite system. A) A series of photographs of thin films spin coated and annealed at 70* °C *under nitrogen, prepared by mixing a colloidal solution with a colloid-free solution B) Hydrodynamic size distribution measured via dynamic light scattering of various perovskite solutions prepared via colloidal mixing of solution.*

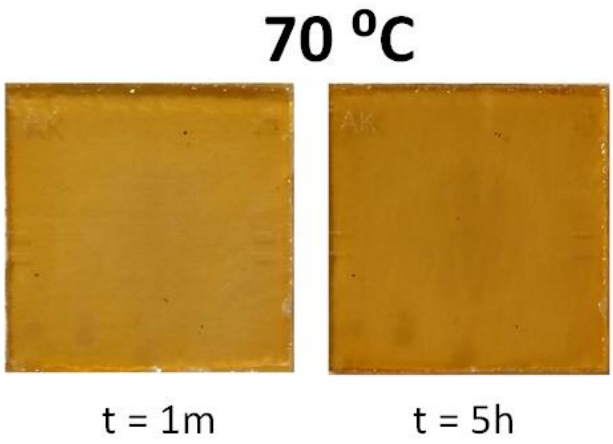

Fig. S5 Nucleation time dependence. $FA_{0.83}Cs_{0.17}Pb(Br_{0.2}I_{0.8})_3$ perovskite films prepare with a colloid-free solution annealed at 70 °C in nitrogen for 1 minute and for 5 hours. Both thin films show no signs of formation of the black perovskite phase.

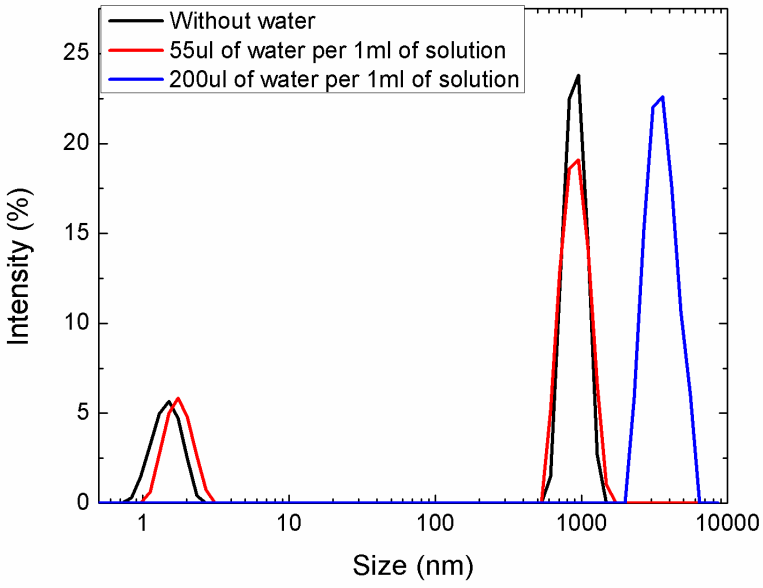

Fig. S6 *Hydrodynamic size distribution measured via dynamic light scattering of perovskite solutions without any additive and perovskite solutions with a water additive.*

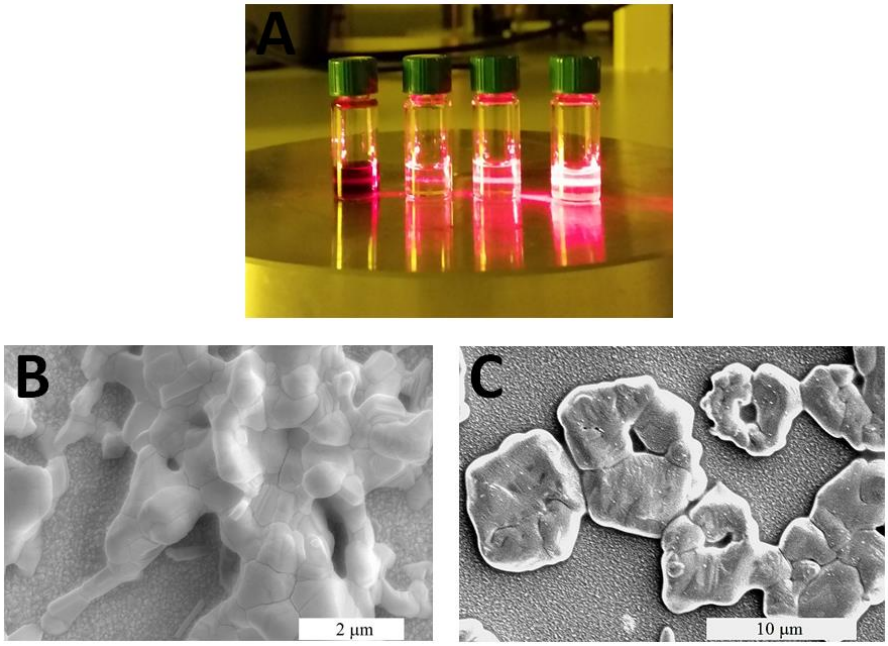

Fig. S7: Impact of bromine/idodine (Br_2/I_2) halides and Hypophosphorous acid (HPA) as additives on the $FA_{0.83}Cs_{0.17}Pb(Br_{0.2}I_{0.8})_3$ perovskite system. A) A photograph of a series of 1.15M $FA_{0.83}Cs_{0.17}Pb(Br_{0.2}I_{0.8})_3$ perovskite solutions containing different additives shined with a red laser showing various degrees light scattering. The additives were added immediately before taking the photograph. From left to right, perovskite solutions were added with I_2/Br_2 (78.5mg/mL and 4µl/mL), HI/HBr (81.7µL/mL and 17.6µL/mL), HPA (200µL/mL), without any additives. B) A series of top-view scanning electron microscope (SEM) images of a fully annealed $FA_{0.83}Cs_{0.17}Pb(Br_{0.2}I_{0.8})_3$ perovskite thin film with I_2/Br_2 and C) HPA as additives.

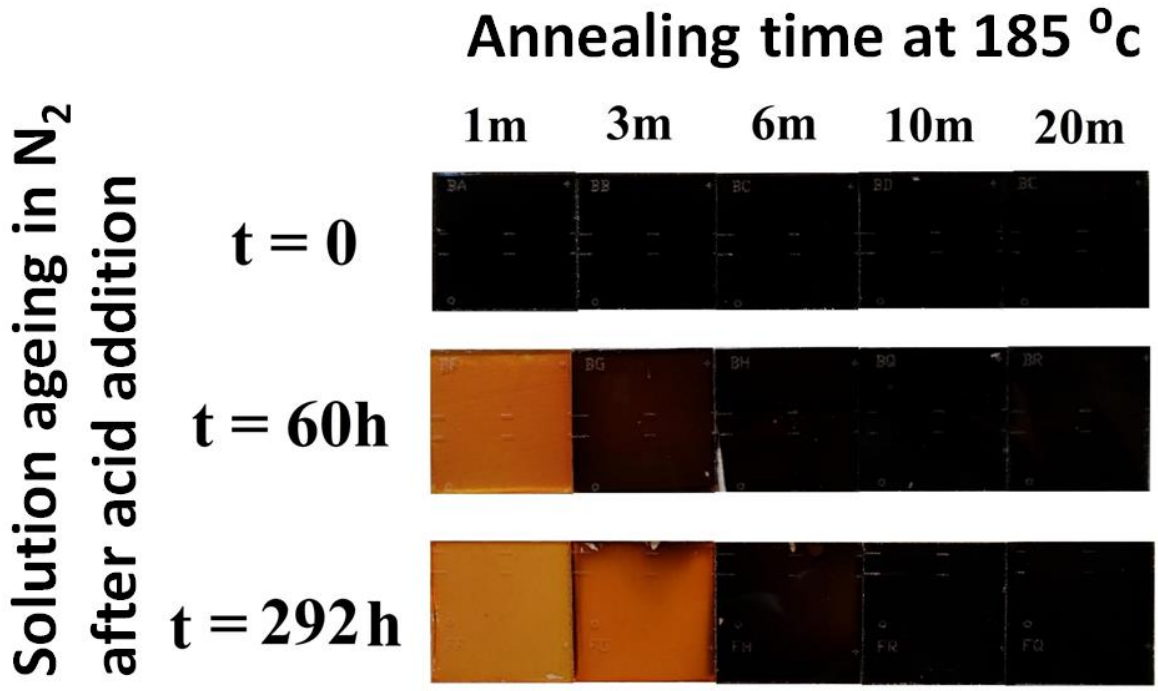

Fig. S8 Photographs of a series of $FA_{0.83}Cs_{0.17}Pb(B_{0.2}rI_{0.8})_3$ thin films when heated at 185 °C in air on a hot plate. The thin films were fabricated using precursor solutions that have been aged for 0h, 60h and 292h after the addition of the hydrohalic acids.

Modified Williamson-Hall method for microstrain estimation

Broadening and shifts in the XRD peak can be caused by either a reduction in the grain size (Scherrer broadening) and/or non-uniform strain (microstrain). We note that Scherrer broadening will only be significant when the grains are in the range of or less than 100 nm, and as we will discuss later we do not expect this to be a significant contribution here. Strain is the relative change in size of an object with respect to its ideal size (or size before experiencing an external force). The microstrain in a crystalline material is a result of small fluctuations in the lattice spacing, induced by crystal imperfections/structural defects including dislocations, vacancies, stacking faults, interstitials, twinning, and grain boundaries.[1,2],[3] By simply

considering Braggs law for scattering of light of wavelength λ, nλ = 2dsinθ, it is clear that small fluctuations in d spacing (i.e. Δd) will result in small fluctuations, or broadening, in θ when measuring the X-ray diffraction from the material. We quantify the extent of microstrain in our perovskite crystals by analysing the peak broadening in the diffraction patterns according to the modified Williamson-Hall method.[2,4] The effective observed d-space broadening (Δd_{obs}) determined from the XRD peak width broadening, is a convoluted function of the Gaussian full width half maximum broadening in the 2θ scan due to the instrument response (Δd_{ins}), the grain size (Δd_{size}) and the microstrain (Δd_{ε}). These can be de-convoluted from the observed broadening, via,

$$\Delta d^2_{obs} = \Delta d^2_{\varepsilon} + \Delta d^2_{ins} + \Delta d^2_{size} \quad (1)$$

where the unit-less microstrain ε is defined as $\varepsilon = (\Delta d_{\varepsilon}/d)$, where d is the mean d-spacing.

For single crystals, the size effect induced peak width broadening can be neglected, hence if $\Delta d^2_{size} << \Delta d^2_{obs}$ [19] and we can write,

$$(\Delta d^2_{obs} - \Delta d^2_{ins})^{1/2} \approx \varepsilon d. \quad (2)$$

Therefore, the slope of $(\Delta d^2_{obs} - \Delta d^2_{ins})^{1/2}$ versus d, gives the magnitude of the microstrain, ε, in the crystals.

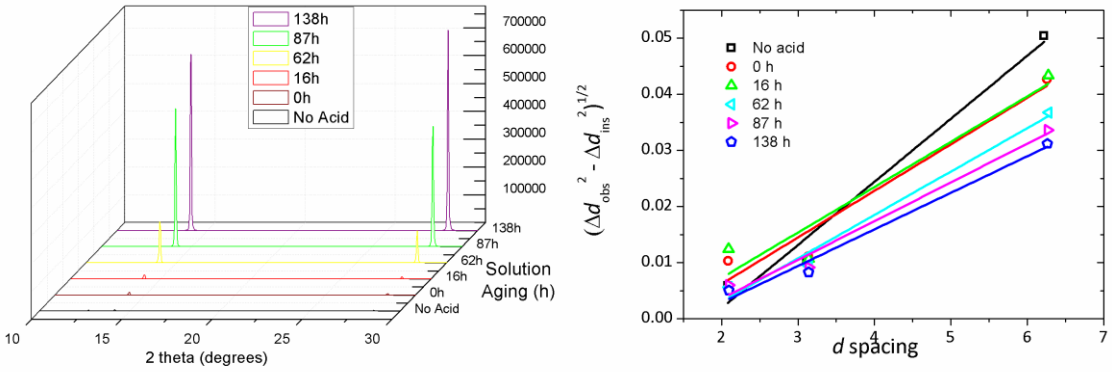

Fig. S9 A) 1D X-ray diffraction pattern of thin films prepared with various precursor solution and annealed at 185 °C B) A modified Williamson-Hall plot of $(\Delta d_{obs}^2 - \Delta d_{ins}^2)^{1/2}$ versus d spacing extracted from the corresponding diffraction profiles shown in Fig. S6A. The slopes of the solid lines from linear fits indicate the extents of microstrain at different doping concentrations.

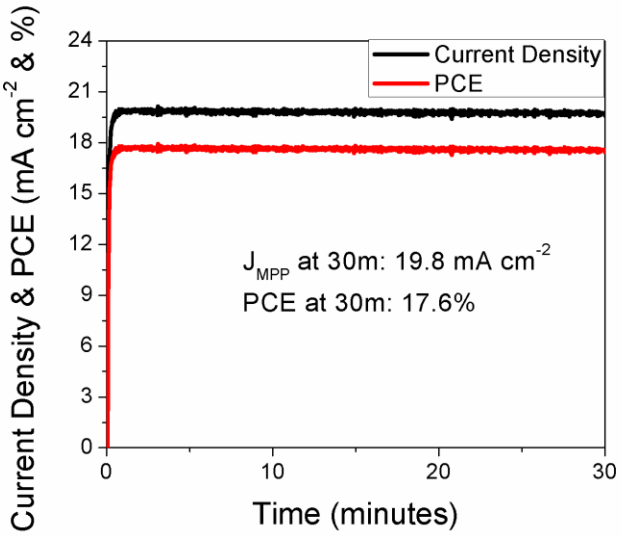

Fig. S10 Photocurrent density and power conversion efficiency of an un-encapsulated device measured in air, under a simulated air-mass (AM) 1.5 100 mW cm^{-2} sun light, held at maximum power voltage for over 30 minutes.

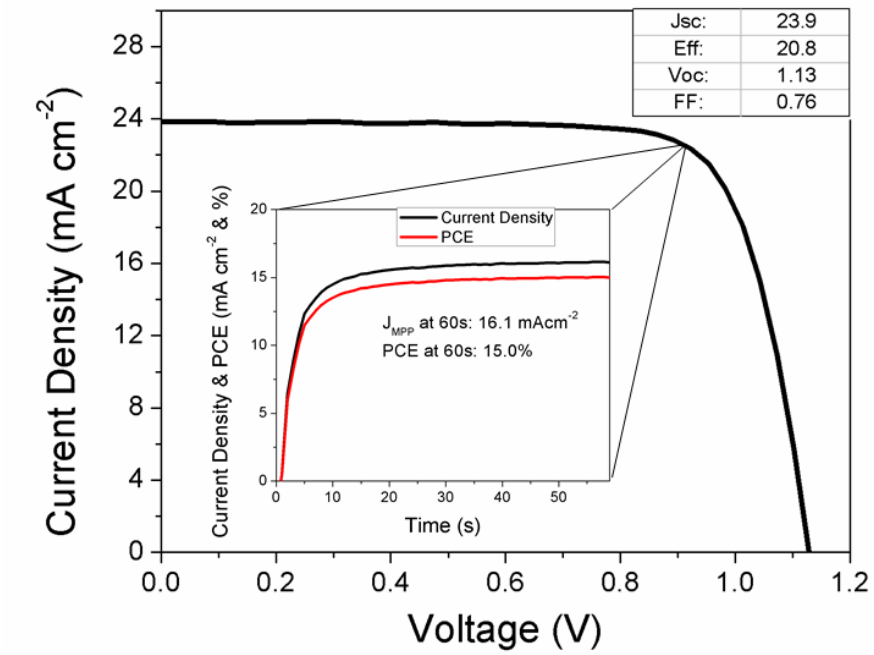

Fig. S11 Forward bias to short-circuit I-V curve for the best scanned efficiency $FA_{0.83}Cs_{0.17}Pb(Br_{0.2}I_{0.8})_3$ perovskite device fabricated with FTO/SnO2/PCBM/perovskite/Spiro-OMeTAD/Ag architecture, measured under simulated air-mass (AM) 1.5 100 mW cm^{-2} sun light using a 0.38V/s scan rate. The inset figure shows the photocurrent density and power conversion efficiency measured at the maximum power point for a 60s time span.

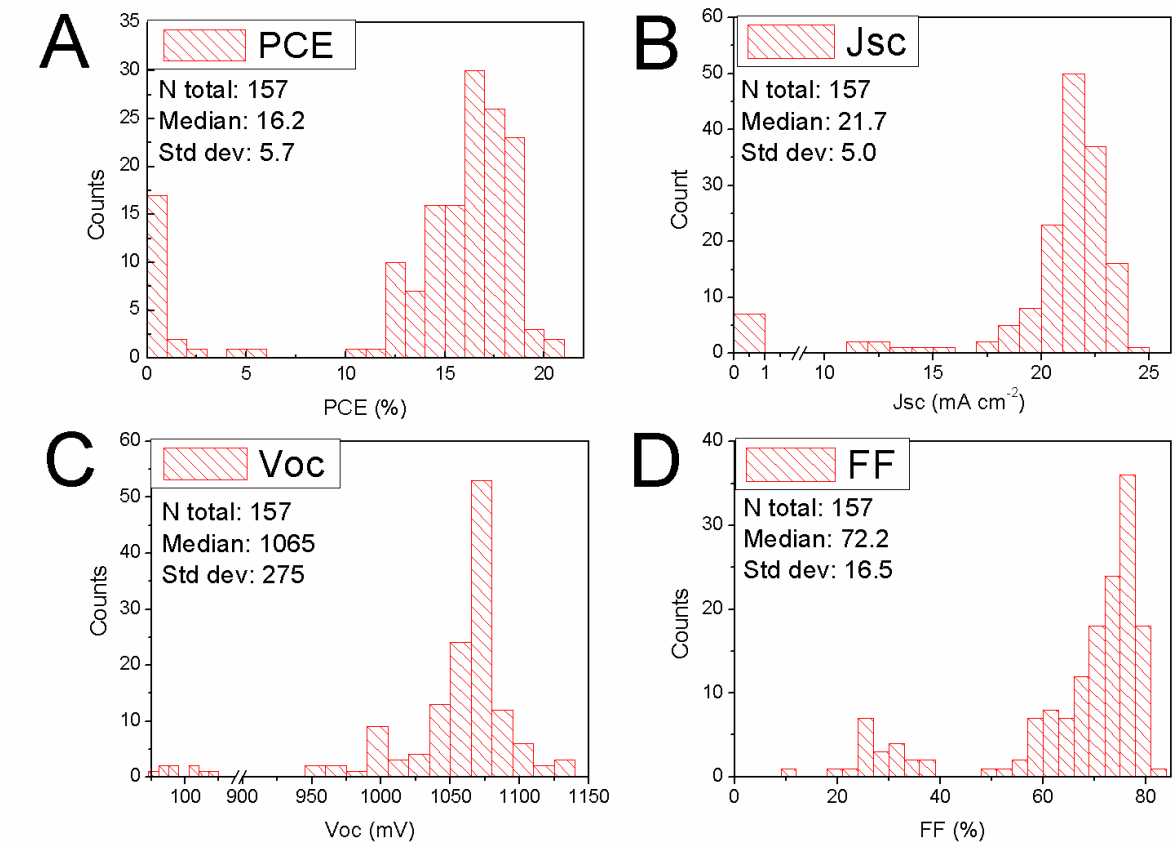

Fig. S12 *Histogram of $FA_{0.83}Cs_{0.17}Pb(I_{0.2}Br_{0.8})_3$ perovskite composition of A) solar cell efficiency B) short-circuit current density C) open-circuit voltage D) Fill-factor*

Supplementary Video *Microscope video (5x speed) using a 50× objective of post-nucleation thin films heated at 220°C in an air atmosphere; prepared using precursor solutions aged with a hydrohalic acid for various period of time.*

Experimental Section

Perovskite precursor synthesis: Formamidinium iodide (FAI) was synthesized by dissolving formamidine acetate salt (99%, Sigma-Aldrich) in a 1.5x molar excess of hydriodic acid (HI), 57 wt. % in H_2O, distilled, stabilized, 99.95% (Sigma-Aldrich). After addition of acid the solution was left stirring for 10 minutes at 50 °C. Upon drying in a large glass dish at 100°C for 2h, a yellow-white powder is formed. This was then washed three times with diethyl ether. The power was later dissolved in ethanol anhydrous ethanol (99.5%, Sigma-Aldrich) heated at 120 °C in a N_2-rich atmosphere to obtain a supersaturate solution. Once fully dissolved, the solution is then slowly cooled at room temperature in a N_2-rich atmosphere, until recrystallization occurs. The recrystallization process forms white flake-like crystals. Afterwards, the solution is then placed and in a refrigerator at 4 °C, and then a freezer for further crystallization. The powder is later washed with diethyl ether three times. Finally, the powder is dried overnight in a vacuum oven at 50 °C.

Perovskite precursor solution mixture: All solutions were dissolved in anhydrous N,N-dimethylformamide (DMF) to obtain a stoichiometric solution with desired composition using precursor salts: formamidinium iodide (FAI), cesium iodide (CsI) (99.9%, Alfa Aesar), lead iodide (PbI_2) (99%, Sigma-Aldrich), lead bromide ($PbBr_2$) (98%, Sigma-Aldrich). 81.7 µl/ml of hydroiodic acid (HI) (57 wt. % in H_2O, distilled, stabilized, 99.95%, Sigma-Aldrich) and 17.6 µl/ml of hydrobromic (HBr) (48 wt. % in H_2O) was added to 1ml of 1.15 M precursor solutions. For precursor solutions with alternate molarities, the volume of both hydrohalic acids was scaled according to the molarity of the solution. After the addition of the acids, the perovskite precursor solution was stored under a nitrogen atmosphere for the desired amount of time.

Perovskite solar cell fabrication: 17.6 µL/mL of HBr (48 wt. % in H2O) and 81.7 µl/ml of HI (57 wt. % in H_2O) was added to a 1.15M $[HC(NH_2)_2]_{0.83}Cs_{0.17}Pb(Br_{0.2}I_{0.8})_3$ precursor perovskite solution. This solution was then aged under a nitrogen atmosphere for approximately 48h. This aged precursor perovskite solution was spin-coated in a nitrogen-filled glovebox at 2000 rpm for 45s, on a substrate pre-heated at 70 °C. The films were dried inside a N_2 glovebox on a hot plate at a temperature of 70 °C for 1 minute. The films were then annealed in an oven in an air atmosphere at 185°C for 120 minutes. During this annealing process, the samples were covered with a large glass container to shield them from any contaminates such as dust particles. For samples annealed at 220°C, the thin films were heated for 10m in air at 220°C. These films were then transferred to a 185°C oven for 110m.

Preparation of tin oxide (SnO_2) nanoparticles: SnO_2 nanoparticles were synthesized via hydrothermal method, similarly to the method described by Zhang et al[5]. We dissolve 467 mg of $SnCl_4 \cdot 5H_2O$ (98%, Sigma-Aldrich) in 20 ml of deionized (DI) water. After 10 minutes of stirring

at room temperature, a fully dissolved, clear solution is obtained. This solution is then transferred to a Teflon-lined stainless steel autoclave, and heated for 2 hours at 200 °C. After heating treatment, the autoclave is quenched to room temperature using cold water. The precipitates were centrifuged at a speed of 9000 rpm for 15 min. The nanoparticles were re-dispersed in ethanol using a spin-coater. This washing treatment was repeated 3 times. After the final washing treatment, the nanoparticles were also re-dispersed in ethanol.

Hole-transporting layer fabrication: The electron-blocking layer was deposited with a 72.5mg/ml of 2,2',7,7'-tetrakis-(N,N-di-p-methoxyphenylamine)9,9'-spirobifluorene (spiro-OMeTAD) (Borun) solution in chlorobenzene. Additives of 24µl of lithium bis(trifluoromethanesulfonyl)imide (170mg/mL in 1-butanol solution) per 1ml of spiro-OMeTAD solution and 7.5µl of 4-tert-butylpyridine (TBP) per 1mL of spiro-OMeTAD solution. The samples were left to oxidize in a desiccator for 48h. Spin-coating was carried out in a nitrogen-filled glovebox at 2000rpm for 60s.

Electron-transporting layer fabrication: Two electron-accepting layers have been discussed in this paper.

1) Tin Oxide(SnO_2)/$PCB_{61}M$: After FTO cleaning process, a 2 mg mL^{-1} SnO_2 nanoparticle solution in anhydrous ethanol (99.5%, Sigma-Aldrich) is spin coated in air on a clean FTO substrate at 2000 rpm for 45s, and annealed at 150 °C for 60s. A 7.5mg ml^{-1} of phenyl-C61-butyric acid methyl ester [60]PCBM (99.5%, Solenne) in anhydrous chlorobenzene (99.8%, Sigma-Aldrich) was later spin coated on top of the SnO_2 layer, in a N_2 glove box at 2000rpm for 45s. The $PCB_{61}M$ was annealed in N_2 atmosphere for 10m.

2) Phenyl-C61-butyric acid benzocyclobutene ester (PCBCB): PCBCB synthesized using the method described by N. Deb et al.[6] After FTO cleaning process, a 3 mg ml^{-1} of PCBCB in anhydrous ethanol (99.5%, Sigma-Aldrich) is spin coated in a N_2 atmosphere on a clean FTO substrate at 2000 rpm for 30s, and annealed in N_2 at 200 °C for 10m.

Electrode: A 50 nm gold electrode was thermally evaporated under vacuum of $\approx 10^{-6}$ Torr, at a rate of ≈ 0.2 nm·s^{-1}.

Device characterization: The current density–voltage (J-V) curves were measured (2400 Series SourceMeter, Keithley Instruments) under simulated AM 1.5 sunlight at 100 $mWcm^{-2}$ irradiance generated by an Abet Class AAB sun 2000 simulator, with the intensity calibrated with an NREL calibrated KG5 filtered Si reference cell. The mismatch factor was calculated to be less than 1%. The active area of the solar cell is 0.0919 cm^{-2}. The forward J–V scans were measured from forward bias (FB) to short circuit (SC) and the backward scans were from short circuit to

forward bias, both at a scan rate of 0.38V s^{-1}. A stabilization time of 5 seconds at forward bias of 1.4 V under illumination was done prior to scanning. The EQE was measured using Fourier transform photocurrent spectroscopy. The EQE was measured in short-circuit (Jsc) configuration following a 1.4V prebias for 5 seconds, using a simulated air-mass (AM) 1.5 100 mW cm^{-2} sun light as illumination source.

Substrate Preparation: Devices were fabricated on fluorine-doped tin oxide (FTO) coated glass (Pilkington, 15Ω $\square^{-1}$). Initially, FTO was removed at specific regions where the anode contact will be deposited. This FTO etching was done using a 2M HCl and zinc powder. Substrates were then cleaned sequentially in Hallmanex detergent, acetone, isopropyl alcohol, and dried with a compressed air gun. The FTO was then cleaned using a "3:1 piranha solution" composed of 3 volume parts of sulfuric acid (H_2SO_4) and 1 volume parts of hydrogen peroxide (H_2O_2) for 90 mins. The FTO was then rinsed in two sequential deionized water (DI) water baths and dried with a compressed air gun.

X-ray diffraction: The one-dimensional and two-dimensional X-ray diffraction spectra of the prepared films were measured using a Rigaku SmartLab X-ray diffractometer with $CuK_{\alpha 1}$ (1.54060 Å) and a HyPix-3000 2D hybrid pixel array detector. All the perovskite films for XRD measurement were deposited on FTO coated glass substrates.

Dynamic Light Scattering: The dynamic light scattering (DLS) was measured using a Malvern Zetasizer Nano ZS. The measurement was done with a quartz cuvette at room temperature.

Optical pump - THz probe spectroscopy: The optical-pump-THz-probe setup uses a Spectra Physics Ti:Sapphire regenerative amplifier to generate 40 fs pulses at a center wavelength of 800 nm and a repetition rate of 1.1 kHz. Terahertz pulses were generated by optical rectification in a 450 µm thick GaP(110) single crystal and detected by electro-optic sampling in a ZnTe crystal (0.2 mm (110)-ZnTe on 3 mm (100)-ZnTe). Pulses for optical excitation of the samples at 400 nm have been generated using a beta barium borat frequency doubling crystal. Optical excitation was carried out from the substrate side of the film. The diameters of optical pump and THz probe beams at the sample position were 3.6 mm and 2.4 mm (FWHM), respectively. Measurements were performed with the entire THz beam path (including emitter, detector and sample) in an evacuated chamber at a pressure of $<10^{-2}$ bar.

Derivation of photoconductivity and charge carrier mobility from change in THz electric field transmission

Assuming the thickness of the perovskite film is smaller than the THz wavelength, the sheet photoconductivity ΔS of a thin film between two media of refractive indices n_a and n_b can be expressed as

$$\Delta S = -\varepsilon_0 c\,(n_a + n_b)\frac{\Delta T}{T} \tag{3}$$

where the product $\varepsilon_0\ c$ denotes the invert of the vacuum impedance and $\Delta T/T$ the photoinduced change in THz electric field transmission over total transmission. As the experiment has been performed in an evacuated box under vacuum, the films are surrounded by vacuum from one side (n_b = 1) and in direct contact with the z-cut quartz substrate from the other side (n_a = 2.13) through which the photoexcitation of the sample occurs.

The charge-carrier mobility μ can be calculated as follows

$$\mu = \frac{\Delta S\ A_{eff}}{N\ e} \tag{4}$$

where ΔS is the sheet photoconductivity of a thin film, e is the elementary charge and N is the number of photoexcited charge-carriers. A_{eff} is the effective area of the overlap of optical pump and THz probe pulse calculated as follows

$$A_{eff} = \frac{\pi}{\ln(2)}\,(FWHM_{pump}^2 + FWHM_{probe}^2) \tag{3}$$

The number of photoexcited charge-carriers N can be determined as follows

$$N = \varphi\frac{E\lambda}{hc}\,(1 - R_{pump})\,(1 - T_{pump}) \tag{4}$$

where φ is the ratio of charge-carriers produced following photon absorption, also known as the photon-to-charge branching ratio, which is assumed to be unity. E, is the energy contained in an optical excitation pulse of wavelength λ, R_{pump} is the reflectivity of the sample at normal incidence of the excitation beam, T_{pump} denotes for the portion of pump beam which is transmitted through the sample. As φ is declared unknown, we define an effective mobility $\tilde{\mu}$ = $\varphi\mu$ which can be directly obtained from our experiments

$$\varphi\mu = -\varepsilon_0 c\,(n_a + n_b)\frac{A_{eff}\,hc}{E\,e\,\lambda\,(1-R_{pump})\,(1-T_{pump})}\frac{\Delta T}{T} \quad (5)$$

The ascertained charge-carrier mobility contains contributions from both electrons and holes. Hence, the derived values for mobility represent the sum of electron and hole mobilities. As φ ranges between 0 and 1, the effective mobility describes a lower limit.

Furthermore, the effective carrier mobilities have been corrected by scaling the onset value of $\frac{\Delta T}{T}$ with the relative surface coverage of the respective films, which were obtained by processing SEM images. The surface coverage procedure suffices our requirements to account for actual effective carrier mobilities in the films as we rule out any excess absorption in possibly thicker films. Due to high absorption coefficients most of the light is being absorbed within the first hundreds of nanometers, for which reason a thickness correction is not required, especially since the thickness of all measured films exceeds 400 nm.

References

[1] I. Robinson, R. Harder, *Nat. Mater.* **2009**, *8*, 291.

[2] A. Pramanick, X. P. Wang, C. Hoffmann, S. O. Diallo, M. R. V. Jørgensen, X.-L. Wang, *Phys. Rev. B* **2015**, *92*, 174103.

[3] G. . Williamson, W. . Hall, *Acta Metall.* **1953**, *1*, 22.

[4] Y. Zhao, J. Zhang, *J. Appl. Crystallogr.* **2008**, *41*, 1095.

[5] Y. Zhang, L. Li, J. Zheng, Q. Li, Y. Zuo, E. Yang, G. Li, *J. Phys. Chem. C* **2015**, *119*, 19505.

[6] N. Deb, R. R. Dasari, K. Moudgil, J. L. Hernandez, S. R. Marder, Y. Sun, A. Karim, D. G. Bucknall, **n.d.**, DOI 10.1039/c5ta05824d.